

## **Effects of Interfacial Velocity Boundary Condition on Turbulent Mass Transfer at High Schmidt Numbers**

Yosuke Hasegawa and Nobuhide Kasagi

Department of Mechanical Engineering, The University of Tokyo

7-3-1 Hongo, Bunkyo-ku, Tokyo 113-8656, Japan

hasegawa@thtlab.t.u-tokyo.ac.jp, kasagi@thtlab.t.u-tokyo.ac.jp

Abstract - Numerical simulation of high Schmidt number turbulent mass transfer across free and solid surfaces is carried out. Near a free surface, the concentration field quickly responds to the normal velocity fluctuation and the eddy diffusivity is almost unchanged even at high Schmidt numbers. In contrast, near a solid wall, the concentration field becomes less sensitive to the normal velocity fluctuation and the eddy diffusivity is drastically decreased with increasing the Schmidt number. This fundamental difference between the concentration fields close to free and solid surfaces can be attributed to the difference in the asymptotic behavior of velocity fluctuations toward the interfaces. Namely, the normal velocity varies quadratically with the distance from a solid surface, while linearly near a free surface. Strong damping of high-frequency concentration fluctuations near a solid surface agrees well with the theoretical analysis by Shaw and Hanratty (AIChE J. 23 (1977a) 160-169). As a result, lower-frequency velocity fluctuations dominate the mass transfer at higher Schmidt numbers. These results imply that the analogy between momentum and mass transfer, which has been widely used in engineering applications, may not hold.

Keyword: turbulence, mass transfer, Schmidt number, interface

## Notation

$A_i$	coefficient for the $i$ -th order in Taylor expansion of eddy diffusivity $E_d$
$a_i$	coefficient for the $i$ -th order in Taylor expansion of streamwise velocity fluctuation $u'$
$B_i$	coefficient for the $i$ -th order in Taylor expansion of eddy diffusivity $E_v$
$b_i$	coefficient for the $i$ -th order in Taylor expansion of surface-normal velocity fluctuation $v'$
$C$	mean concentration
$C_B$	bulk mean concentration
$C_I$	mean concentration at an interface
$D$	molecular diffusivity
$E_d$	eddy diffusivity
$E_v$	eddy viscosity
$K$	mass transfer rate
$k_B$	Batchelor wave number
$k_x, k_y, k_z$	number of modes in streamwise, surface-normal and spanwise directions
$p$	pressure
$Q$	mean mass flux at an interface
$q$	local mass flux at an interface
$R_{\alpha\beta}$	correlation coefficient between $\alpha$ and $\beta$
$Re_\tau$	Reynolds number based on friction velocity $u_\tau$ and depth $\delta$
$N$	number of grid points
$s_i$	coefficient for the $i$ -th order in Taylor expansion of concentration fluctuation $c'$
$Sc$	Schmidt number
$Sc_t$	turbulent Schmidt number
$t$	time
$U$	mean streamwise velocity
$u, v, w$	velocity components in the $x, y,$ and $z$ directions
$u_\tau$	friction velocity
$W_\alpha$	frequency spectrum of fluctuating component $\alpha$
$W_{cv}$	frequency co-spectrum of $\overline{c'v'}$
$x, y, z$	streamwise, surface-normal and spanwise directions

$y_p$  peak location of concentration fluctuation

*Greek*

$\beta$  coefficient for the first order in Taylor expansion of normal velocity fluctuation

$\gamma$  coefficient for the second order in Taylor expansion of normal velocity fluctuation

$\Delta C$  difference between concentrations at an interface and a bottom boundary

$\Delta C_B$  difference between the interfacial and bulk concentrations

$\Delta_d$  thickness of the diffusive sublayer

$\Delta t$  time step

$\Delta x, \Delta y, \Delta z$  grid spacings in streamwise, surface-normal and spanwise directions

$\delta$  depth of computational domain

$\delta_c$  thickness of the concentration boundary layer

$\nu$  kinematic viscosity

$\rho$  fluid density

$\omega$  frequency

*Superscript*

$()^*$  dimensional value

$()^+$  value non-dimensionalized by the shear unit

$()'$  fluctuating component

$\overline{()}$  mean component

*Subscript*

$()_a$  value in the air phase

$()_w$  value in the water phase

## 1. Introduction

Heat and mass transfer across free and solid surfaces plays an important role in a variety of engineering applications and also in many environmental problems. When considering mass transfer inside liquid, the Schmidt number is commonly high ( $Sc \sim O(10^3)$ ) and the transport mechanism is governed by turbulent motions within a thin concentration boundary layer in the immediate vicinity of a surface ( $\delta_c \sim O(10-100 \mu\text{m})$ ).

In the previous study, Hasegawa and Kasagi (2005) investigated the microscopic transport mechanisms across clean and contaminated air-water interfaces. At the clean interface, the interfacial mass flux quickly responds to the normal velocity fluctuation. With increasing the degree of surface contamination, however, high-frequency concentration fluctuation components are strongly damped. Moreover, the mass transfer rate drastically deteriorates and eventually falls down to the value on a solid wall. Since the normal velocity fluctuation near a highly contaminated interface converges to the data near a solid surface (Hasegawa and Kasagi, 2005), the contaminated interface can be approximated by a solid surface in terms of the mass transfer.

This fundamental difference between the concentration fields close to free and solid surfaces was first discussed by McCready and Hanratty (1984). They argued that a velocity component  $v$  in the surface-normal direction  $y$  plays a critical role in the interfacial mass transfer. By expanding  $v$  in Taylor series as  $v(t,y) = \beta(t)y$  and  $v(t,y) = \gamma(t)y^2$  at free and solid surfaces, respectively, they obtained the following relationships for high frequencies. Namely, for a free surface,

$$W_q(\omega) = \frac{W_\beta(\omega)}{\omega^2} Q^2, \quad (1)$$

whereas, for a solid surface (Shaw and Hanratty, 1977a),

$$W_q(\omega) = \frac{4W_\gamma(\omega)}{Sc \cdot \omega^3} Q^2. \quad (2)$$

Here,  $W_q$ ,  $W_\beta$  and  $W_\gamma$  are the frequency spectra of the interfacial mass flux  $q$  and the normal velocity fluctuations near free and solid surfaces, respectively. The above equations imply the concentration fluctuation near a solid surface is damped faster than

that near a free surface with increasing the frequency  $\omega$ . Furthermore, the appearance of  $Sc$  in the denominator of Eq. (2) reveals that the damping near a solid surface is more enhanced at higher Schmidt numbers. Although high Schmidt number effects near free and solid surfaces should be quite different, few studies have focused on this issue.

The damping effect on concentration fluctuations near a solid surface has a strong impact on the limiting behavior of an eddy diffusivity  $E_d$ . Since the mean concentration profile mostly changes inside the viscous sublayer at high Schmidt numbers, Taylor series have been usually employed for representation of velocity and concentration fields. Considering that both the eddy diffusivity  $E_d$  and the eddy viscosity  $E_v$  vary as  $y^3$  near a solid surface, the analogy between momentum and mass transfer has been well documented (e.g., Monin and Yaglom, 1971; Kader, 1981; Churchill, 1997), i.e.,  $E_d \sim A_3 y^3$ , where the proportional constant  $A_3$  is assumed independent of the Schmidt number. This leads to a well-known relationship of  $K^+ = K / u_\tau \propto Sc^{-2/3}$ , where  $K$  is the mass transfer rate and  $u_\tau$  is the friction velocity.

According to the precise experiments with an electrochemical technique conducted by Shaw and Hanratty (1977b), however,  $K^+$  was proportional to  $Sc^{-0.7}$ . They also observed that the contribution of large wavenumbers to turbulent mass flux is strongly damped with increasing the Schmidt number. This trend agrees with the theoretical analysis given by Eq. (2).

Recently, numerical simulation of turbulent mass transfer across a solid surface has also been carried out. Such simulations are quite useful in providing the detailed statistics of velocity and concentration fields near a solid surface, which can not be obtained in experiments. Papavassiliou and Hanratty (1997) applied a Lagrangian method to turbulent mass transfer at up to  $Sc = 2400$  and reported that  $E_d$  is represented by  $E_d \propto y^{3.38}$  rather than  $y^3$  inside the concentration boundary layer. Although the Lagrangian approach is useful in obtaining mean concentration profiles, it is not straightforward to obtain higher-order statistics.

Calmet and Magnaudet (1997) carried out large eddy-simulation (LES) of high Schmidt number mass transfer in turbulent channel flow and showed that large-scale structures govern the mass transfer. Direct numerical simulation (DNS) by Na and Hanratty (2000) reported that the limiting value of  $E_d / y^3$  at a solid wall decreases by about 30 % with increasing the Schmidt number from 1.0 to 10. Recent high-resolution DNS data by Seki et al. (2006) also support this trend. These results suggest the

breakdown of analogy between momentum and mass transfer at high Schmidt numbers. Therefore, there has been strong need to investigate the limiting behavior of the concentration and velocity fields close to a solid surface. However, most existing DNS databases are limited to low to moderate Schmidt numbers ( $Sc \sim O(10)$ ).

In this work, we carry out numerical simulation of turbulent mass transfer at  $Sc = 100$  across two distinct boundaries, *i.e.*, a clean air-water interface and a solid surface. In order to calculate the concentration field at the high Schmidt number, we apply a hybrid DNS/LES scheme, which employs DNS with high-resolution grids within the concentration boundary layer, while large-eddy simulation (LES) with coarser grids in the outer layer.

Our main objective is to clarify the effects of the velocity boundary condition on high Schmidt number turbulent mass transfer inside the viscous sublayer. Specifically, we examine high Schmidt number effects on the limiting behavior of the eddy diffusivity and the damping of concentration fluctuations with the two kinds of boundary conditions.

## 2. Computational Model and Numerical Method

### 2.1 Numerical conditions

We consider two flow conditions as shown in Figs. 1 (a) and (b). The first case is a fully developed counter-current air-water flow driven by a constant pressure gradient as shown in Fig. 1 (a), where  $x$ ,  $y$  and  $z$  are the streamwise, surface-normal and spanwise directions, respectively. The computational periods are chosen to be  $2.5\pi\delta^*$  and  $\pi\delta^*$  in the  $x$  and  $z$  directions, respectively, where  $\delta^*$  is the depth of the computational domain. A value with an asterisk represents a dimensional value throughout the present paper.

The governing equations are the incompressible Navier-Stokes, continuity, and scalar transport equations given below:

$$\frac{\partial u_i}{\partial t} + u_j \frac{\partial u_i}{\partial x_j} = -\frac{\partial p}{\partial x_i} + \frac{1}{Re_\tau} \frac{\partial^2 u_i}{\partial x_j \partial x_j}, \quad (3)$$

$$\frac{\partial u_i}{\partial x_i} = 0, \quad (4)$$

$$\frac{\partial c}{\partial t} + u_j \frac{\partial c}{\partial x_j} = \frac{1}{Re_\tau \cdot Sc} \frac{\partial^2 c}{\partial x_j \partial x_j}, \quad (5)$$

where, the velocity  $u_i$  and the coordinate  $x_i$  are non-dimensionalized by  $u_\tau^*$  and  $\delta^*$  in each phase, where  $u_\tau^*$  is the interfacial friction velocity. The concentration  $c^*$  of a solute is normalized by the concentration difference  $\Delta C^*$  between the free surface and the bottom boundary in the water phase. The non-dimensional parameters which characterize the velocity and concentration fields are the Reynolds number  $Re_\tau = u_\tau^* \delta^* / \nu^*$  and the Schmidt number  $Sc = \nu^* / D^*$ , where  $\nu^*$  and  $D^*$  are the kinematic viscosity and the molecular diffusivity of a gaseous solute, respectively. The Reynolds numbers based on  $u_\tau^*$  and  $\delta^*$  in the air and water phases are  $Re_{\tau w} = Re_{\tau a} = 150$ , which approximately corresponds to an air-water flow with  $u_a^* = 2.2$  m/s and  $u_w^* = 0.054$  m/s at two outer boundaries of  $\delta^* = 4$  cm. The subscripts  $a$  and  $w$  represent values in the air and water phases, respectively. The density ratio of water and air is  $\rho_w^* / \rho_a^* = 841$ .

Since we focus on the fundamental difference between slip and no-slip boundary conditions at free and solid surfaces in terms of the mass transfer, interfacial deformation is neglected to avoid additional complexity. Hence, the resultant velocity boundary condition at the air-water interface is the continuity of horizontal velocity components as well as the shear stress.

$$u_{iw} = \sqrt{\frac{\rho_w}{\rho_a}} u_{ia} \quad (i = 1 \text{ and } 3) \quad (6)$$

$$u_{2w} = u_{2a} = 0 \quad (7)$$

$$\frac{1}{Re_{\tau_w}} \frac{\partial u_{iw}}{\partial x_{2_w}} = \frac{1}{Re_{\tau_a}} \frac{\partial u_{ia}}{\partial x_{2_a}} \quad (i = 1 \text{ and } 3) \quad (8)$$

Hereafter, we will focus on only the water phase and omit the subscript of  $w$ .

In the second case, the air-water interface is replaced by a no-slip boundary as shown in Fig. 1 (b). Hence, the interfacial velocity boundary conditions are given as:

$$u_1 = u_2 = u_3 = 0 \quad (9)$$

In both cases, a free-slip condition is used at the bottom boundary. For the concentration field, a constant concentration boundary condition  $c = 1$  is imposed at the interfaces, while  $c = 0$  at the bottom. The Schmidt number  $Sc$  is set to be 1.0 and 100 in each case.

Direct numerical simulation (DNS) is applied to the velocity and concentration fields at  $Sc = 1.0$  by using a pseudo-spectral method. 64 x 64 Fourier

modes in the  $x$  and  $z$  directions and Chebyshev polynomials up to 289 in the  $y$  direction are used. For time integration, the second-order Adams-Bashforth and Crank-Nicolson schemes are adopted for the nonlinear and diffusion terms, respectively. For the high Schmidt number of 100, a hybrid DNS/LES scheme described below is employed.

## 2.2 Hybrid DNS/LES scheme

Since the concentration dissipation wave number, *i.e.*, the Batchelor wave number  $k_B$ , is generally proportional to  $Sc^{1/2}$  (Batchelor, 1959),  $N^3 \propto Sc^{3/2}$  computational grids are required in order to resolve all essential scales of the concentration field. In the case of the interfacial mass transfer, most concentration change occurs in the vicinity of the interface. Therefore, for a concentration field at  $Sc = 100$ , we apply a hybrid DNS/LES method, which employs DNS with high-resolution grids within a near-interface region  $y^+ < 11.3$ , while LES with coarser grids for the outer layer  $y^+ > 21.5$ . We provide a switching region between them in order to connect the two regions smoothly. The depth of the DNS region is determined so that more than 95 % of the mean concentration change should be resolved by DNS. For spatial discretization, Fourier series are used in the  $x$  and  $z$  directions, and the finite volume method is employed in the  $y$  direction. Turbulent and molecular mass fluxes in the  $y$  direction are evaluated at a surface of a control volume in the second-order accuracy. In the DNS and switching regions, Fourier modes up to 8 times that for the velocity field are employed in the  $x$  and  $z$  directions, whereas in the LES region, the same grid system as that for the velocity field is used. Since the finer computation grid is employed for the concentration field in the DNS and switching regions, the fluid velocity calculated on the coarser grid should be appropriately interpolated onto the finer grids in order to evaluate the convective terms. In this study, a Fourier interpolation scheme, namely, the fast Fourier transform (FFT) with higher wavenumber components set to be zero, is employed for the  $x$  and  $z$  directions.

When we employ the hybrid DNS/LES scheme, we note the following issues:

1. Depth of DNS region
2. Grid resolution in DNS region
3. Subgrid-scale model in LES region

We study the first and second issues by running computations with different depths of the DNS region (Cases 1 and 2) and different grid resolutions (Cases 1 and 3). Computational conditions are listed in Table I.

As for the subgrid mass-flux model in the LES region, we employ the Dynamic Smagorinsky Model (DSM), in which an unknown coefficient is calculated by Germano identity with the double-filtering procedure (Germano et al., 1991). It is possible to use more complex models such as the Dynamic Mixed Model (DMM) (Zang et al., 1993) and the Dynamic Two-parameter Model (DTM) (Salvetti and Banerjee, 1995). It should be noted, however, that the most concentration change occurs in the DNS region and the contribution of the subgrid-scale mass flux on the total mass transfer is found to be quite small, i.e., less than 3 %, over the whole domain. Therefore, the effect of the subgrid model on the total mass transfer is considered to be insignificant. Details of the numerical scheme can also be found in Hasegawa and Kasagi (2005 and 2007).

The time increment is  $\Delta t^+ = 0.018$  in Cases 1 and 2, while  $\Delta t^+ = 0.012$  in Case 3, all of which are small enough to satisfy the Courant condition for solving the concentration field. In order to obtain the statistics of velocity and concentration fields, time integration is repeated for  $t^+ = 2000$  after the velocity and concentration fields reached the statistically stationary state.

### 3. Results

#### 3.1 Statistics of concentration field

The flow statistics under the present flow conditions have already been reported in Lombardi et al. (1996) and Hasegawa and Kasagi (2005). The mean concentration profiles near the free and solid surfaces at  $Sc = 100$  are presented in Fig. 2. The abscissa is the distance from the interface in the shear unit. The ordinate is the mean concentration relative to the interfacial concentration non-dimensionalized by the friction concentration. A distinct difference between the mean profiles near the free and solid surfaces can be found. The mass transfer rate  $K^+$  is defined as:

$$K^+ = \frac{Q^*}{u_\tau^*} = \frac{Q^*}{u_\tau^* (C_I^* - C_B^*)} = \frac{1}{\Delta C_B^+}. \quad (10)$$

Here,  $Q^*$ ,  $C_I^*$  and  $C_B^*$  are the mean mass flux and the mean concentrations at the interface and the bulk, respectively, while  $\Delta C_B^* = C_I^* - C_B^*$ . In the present calculation,  $K^+ = 0.0096$  and  $0.0032$  at the free and solid surfaces, respectively. These values agree reasonably well with the experimental results, i.e.,  $K^+ = 0.12Sc^{-0.5}$  at a sheared air-water interface (Hanratty, 1991) and  $0.0889Sc^{-0.704}$  at a solid surface (Shaw and Hanratty, 1977b). Slight underestimate of  $K^+$  at the free surface may be attributed to the neglect of surface waves and turbulence generation at a bottom wall in the present calculation. The present data at the solid surface also underestimates  $K^+$  by 8 %. This probably stems from the low Reynolds number considered here.

The thickness  $\Delta_d^+$  of the diffusive sublayer, in which  $C^+ = Sc \cdot y^+$  is satisfied within deviation of 5 %, roughly varies as  $Sc^{-1/2}$  and  $Sc^{-1/3}$  for free and solid surfaces, respectively. Specifically, with increasing  $Sc$  from 1.0 to 100,  $\Delta_d^+$  changes from 2.9 to 0.28 for the free surface, whereas 6.2 to 1.4 for the solid surface. Note that the empirical correlation for a mean concentration profile near the solid surface proposed by Kader (1981) is plotted for comparison. Kader's relationship predicts a thinner diffusive sublayer and a slightly lower concentration away from the interface. This trend is also observed in recent calculations at low Reynolds numbers ( $Re_\tau = 150 \sim 180$ ) by Seki et al. (2006) and Tiselj (2006). These facts suggest a need for modification of the empirical relationship at a low Reynolds number.

The concentration fluctuations  $c_{rms}$ , which are normalized by the difference  $\Delta C_b$  between the interfacial and bulk concentrations, are shown in Figs. 3 (a) and (b), respectively. At  $Sc = 1.0$ , the peak locations  $y_p^+$  near the solid and free surfaces are almost the same, i.e.,  $y_p^+ = 17.8$ . With increasing the Schmidt number from 1.0 to 100, the peak location near the free surface moves closer to the interface, i.e.,  $y_p^+ = 1.1$  and 2.6 at the free and solid surfaces, respectively. Moreover, the peak value near the free surface becomes more prominent at the high Schmidt number. These results suggest that turbulent eddies exist close to the free surface and effectively generate concentration fluctuations.

As a whole, fairly good agreement in the mean and fluctuating concentrations among Cases 1, 2 and 3 is observed. Specifically, the differences in the mass transfer rate  $K^+$  and the peak value of concentration fluctuation between the three cases are less than 2 %. The boundaries between the DNS, switching and LES regions in Case 1 are depicted in Figs. 2 and 3. By inserting the switching region, we obtained a smooth mean concentration profile (see, Fig. 2). Although slight bump is observed at the connection between the switching and LES regions in the profile of the concentration fluctuation, comparison between Cases 1 and 2 shows that the depth of the DNS region does not influence the concentration field close to the interface. The peak location of the concentration fluctuation at  $Sc_w = 100$  in Case 1 corresponds to the 11th and 17th grid points from the free and solid surfaces, respectively. Hence, the present grid resolution in the  $y$  direction is fine enough to resolve the sharp peak. These results indicate that the grid resolution is sufficient and the depth of the DNS region is large enough to calculate the concentration statistics. Hereafter, we show the concentration statistics obtained in Case 1.

Figures 4 (a) and (b) present the correlation coefficients  $-R_{cu}$  and  $R_{cv}$  between the concentration and the streamwise/normal velocity fluctuations. Distinct differences in  $-R_{cu}$  and  $R_{cv}$  between free and solid surfaces become apparent in the neighborhood of the surface. At  $Sc = 1.0$ ,  $-R_{cu}$  is quite high near the solid surface due to similarity in the boundary conditions, i.e.,  $u' = 0$  and  $c' = 0$ , as well as the governing equations. With the Schmidt number increased,  $-R_{cu}$  is decreased near both free and solid surfaces. Especially, the decrease of  $-R_{cu}$  near the solid surface is significant. An interesting feature of the free surface is that  $R_{cv}$  is kept high  $\sim 0.6$  even at the high Schmidt number

(see, Fig. 4 (b)). In contrast, near the solid surface,  $R_{cv}$  is drastically decreased at the high Schmidt number.

These results indicate that the concentration field near a solid surface becomes less sensitive to the normal velocity fluctuations with increasing the Schmidt number, whereas, near a free surface, the concentration field quickly responds to the normal velocity fluctuation at a wide range of Schmidt numbers.

### 3. 2 Limiting behavior of eddy diffusivity near free and solid surfaces

Since the most concentration change occurs close to a surface at high Schmidt numbers, the limiting behavior of concentration and velocity fields is of particular importance for modeling mass transfer. Considering Eqs. (6-8) and a constant concentration condition at a free surface, the fluctuating velocity and concentration fields can be expanded in Taylor series as follows:

$$c^{+'} = s_1 y^+ + s_3 y^{+3} + O(y^{+4}), \quad (11)$$

$$u^{+'} = a_0 + a_1 y^+ + O(y^{+2}), \quad (12)$$

$$v^{+'} = b_1 y^+ + b_2 y^{+2} + O(y^{+3}). \quad (13)$$

Note that there is no  $y^2$  term in the equation of  $c^{+'}$  because  $\partial^2 c' / \partial y^2$  should be identically zero at an iso-concentration boundary. The asymptotic expressions for the turbulent mass flux  $\overline{c^{+'} v^{+'}}$  and the turbulent momentum flux  $\overline{u^{+'} v^{+'}}$  are also given as:

$$\overline{c^{+'} v^{+'}} = \overline{s_1 b_1} y^{+2} + \overline{s_1 b_2} y^{+3} + O(y^{+4}), \quad (14)$$

$$\overline{u^{+'} v^{+'}} = \overline{a_0 b_1} y^+ + \overline{(a_0 b_2 + a_1 b_1)} y^{+2} + O(y^{+3}). \quad (15)$$

Similarly, considering no-slip and constant concentration conditions, the following expressions are obtained for the solid surface:

$$c^{+'} = s_1 y^+ + s_3 y^{+3} + O(y^{+4}), \quad (16)$$

$$u^{+'} = a_1 y^+ + a_2 y^{+2} + O(y^{+3}), \quad (17)$$

$$v^{+'} = b_2 y^{+2} + b_3 y^{+3} + O(y^{+4}), \quad (18)$$

$$\overline{c^{+'}v^{+'}} = \overline{s_1 b_2} y^{+3} + \overline{s_1 b_3} y^{+4} + O(y^{+5}), \quad (19)$$

$$\overline{u^{+'}v^{+'}} = \overline{a_1 b_2} y^{+3} + \overline{(a_1 b_3 + a_2 b_2)} y^{+4} + O(y^{+5}). \quad (20)$$

The eddy diffusivity  $E_d^+$  and the eddy viscosity  $E_v^+$  are defined as:

$$E_d^+ = -\overline{c^{+'}v^{+'}} / \left( \frac{\partial C^+}{\partial y^+} \right), \quad (21)$$

$$E_v^+ = -\overline{u^{+'}v^{+'}} / \left( \frac{\partial U^+}{\partial y^+} \right). \quad (22)$$

Since the mean concentration and the mean streamwise velocity can be expanded as

$C^+ = Sc \cdot y^+ + O(y^{+2})$  and  $U^+ = y^+ + O(y^{+2})$ , respectively, the limiting behavior of  $E_d^+$

and  $E_v^+$  near the free surface is obtained from Eqs. (14) and (15) as:

$$E_d^+ = A_2 y^{+2} + O(y^{+3}), \quad (23)$$

$$E_v^+ = B_1 y^+ + O(y^{+2}), \quad (24)$$

where  $A_2 = -\overline{s_1 b_1} / Sc$  and  $B_1 = -\overline{a_0 b_1}$ . Similarly, near the solid surface,

$$E_d^+ = A_3 y^{+3} + O(y^{+4}), \quad (25)$$

$$E_v^+ = B_3 y^{+3} + O(y^{+4}). \quad (26)$$

where  $A_3 = -\overline{s_1 b_2} / Sc$  and  $B_3 = -\overline{a_1 b_2}$ .

In Fig. 5, the limiting behavior of  $E_d^+$  and  $E_v^+$  near the free and solid surfaces is represented. Near the free surface,  $E_d^+$  is almost independent of the Schmidt number. On the other hand, near the solid surface,  $E_d^+$  is drastically decreased with the Schmidt number increased. The relation  $E_d^+ = 0.000463 y^{+3.38}$  suggested by Shaw and Hanratty (1977b) based on their experiment at  $Sc = 700$  to  $37000$  is also plotted in Fig. 5. The present result at  $Sc = 100$  decreases faster than  $y^3$  as the solid surface is approached, and excellent agreement with the experimental result can be confirmed.

According to Eq. (25), there should exist a thin layer in which  $E_d^+ \propto y^{+3}$ . In order to investigate more closely, the limiting behavior of  $E_d^+ / y^{+3}$  and  $E_v^+ / y^{+3}$  near the solid surface is shown in Fig. 6. Due to Eqs. (25) and (26), the limiting values of  $E_d^+ / y^{+3}$  and  $E_v^+ / y^{+3}$  at the solid surface should be identical to  $A_3$  and  $B_3$ , respectively. At  $Sc = 1.0$ ,  $E_d^+$  agrees well with  $E_v^+$  in the near-surface region. This confirms the validity of analogy between momentum and mass transfer at  $Sc = 1.0$ .

At  $Sc = 100$ , however,  $A_3$  is decreased by about 80 % with the Schmidt number increased from 1.0 to 100. Moreover, the thickness of the region where  $E_d^+ / y^{+3}$  is constant decreases with increasing the Schmidt number. This suggests that the assumption of constant  $E_d^+ / y^{+3}$  is valid only inside the diffusive sublayer, where the contribution of turbulent transport is quite small compared with that of molecular transport. The similar trend is also reported in Na and Hanratty (2000) at moderate Schmidt numbers up to  $Sc = 10$ . These facts indicate the analogy between momentum and mass transfer at the high Schmidt numbers is not likely to hold. A mean concentration profile calculated by assuming  $E_d^+ = E_v^+$  is plotted with a solid line in Fig. 2. Clear discrepancy with the hybrid DNS/LES data is confirmed.

Limiting values at free and solid surfaces obtained in the present and previous studies are summarized in Table 2. In the case of a solid surface,  $\lim_{y \rightarrow 0} \left\{ \sqrt{c^{+12}} / (C^+ - C_t^+) \right\} = \sqrt{s_1^2} / Sc$  is gradually decreased with increasing the Schmidt number. In contrast, at a free surface,  $\sqrt{s_1^2} / Sc$  is slightly increased with  $Sc$ . This is consistent with the prominent peak of concentration fluctuation near the free surface in Fig. 3 (b).

The turbulent Schmidt number  $Sc_t$  is defined as:

$$Sc_t = \frac{E_v^+}{E_d^+}. \quad (27)$$

The limiting values of  $Sc_t$  are also listed in Table 2 together with the data at  $Sc = 10$  reported by Na and Hanratty (2000) and Seki et al. (2006). Monotonic increase of  $Sc_t$  with  $Sc$  at a solid surface can be confirmed. This corresponds to the drastic decrease of  $E_d^+$  at the high Schmidt number in Fig. 5.

In the following section, we will study frequency spectra of the concentration field close to free and solid surfaces, in order to explain these differences in the Schmidt

number effects between free and solid surfaces.

#### 4. Frequency Spectra at High Schmidt Number

Because of a thin concentration boundary layer at high Schmidt numbers, derivatives in the  $y$  direction are much larger than those in other two directions. Hence, the transport equation near a surface can be simplified as:

$$\frac{\partial c}{\partial t} + v \frac{\partial c}{\partial y} = \frac{1}{Sc} \frac{\partial^2 c}{\partial y^2}. \quad (28)$$

Here, all variables are normalized by the shear units. A fundamental difference between solid and free surfaces is that the normal velocity fluctuation  $v$  varies quadratically with  $y$  near a solid surface, while linearly near a free surface. McCready and Hanratty (1984) explored how the limiting behavior of  $v$  affects the sensitivity of the concentration boundary layer to velocity fluctuations. By substituting  $v = \gamma y^2 \cdot \exp(i\omega t)$  into Eq. (28), the following relationship is obtained for a solid surface:

$$\frac{W_q(\omega)}{Q^2} = \frac{4W_\gamma(\omega)}{Sc \cdot \omega^3}, \quad (29)$$

Similarly, for a free surface, substitution of  $v = \beta y \cdot \exp(i\omega t)$  results in:

$$\frac{W_q(\omega)}{Q^2} = \frac{W_\beta(\omega)}{\omega^2}, \quad (30)$$

where  $W_q$ ,  $W_\gamma$  and  $W_\beta$  are frequency spectra of the interfacial mass flux  $q$ , and  $\beta$  and  $\gamma$ , respectively. Note that Eqs. (29) and (30) are valid only for high frequencies, i.e.,  $Sc \cdot \omega \gg 1$ .

In Figs. 7 (a) and (b),  $W_q$ ,  $W_\gamma$  and  $W_\beta$  at the solid and free surfaces are plotted. Excellent agreement between the present calculation and Eq. (29) is observed for the solid surface (see, Fig. 7 (a)). The appearance of the Schmidt number in the denominator of Eq. (29) explains the strong damping of the concentration fluctuation at high Schmidt numbers. In the case of the free surface, however, the damping of concentration fluctuations at the high Schmidt number is insignificant and the frequency spectrum again agrees fairly well with the theoretical prediction by Eq. (30). Note that Eq. (30) is independent of the Schmidt number.

The damping effect on concentration fluctuation near a solid surface has great

influence on the transport mechanisms. Frequency co-spectrum  $W_{cv}$  of the turbulent mass transport  $\overline{c'v'}$  at  $y^+ = 3.2$  from solid and free surfaces are shown in Figs. 8 (a) and (b), respectively. Here,  $W_{cv}$  is defined as:

$$\overline{c'v'} = \int_{\omega=0}^{\infty} W_{cv} d\omega. \quad (31)$$

Near the solid surface, the contribution of high-frequency fluctuations to the turbulent mass transfer drastically decreases with increasing the Schmidt number. In contrast, near the free surface, the profile is almost unchanged. Although we show the frequency spectra only at a single point here, similar tendency is observed throughout the viscous sublayer, where  $\nu$  varies as  $y$  and  $y^2$  near the free and solid surfaces, respectively.

These results indicate that lower-frequency velocity fluctuations dominate the turbulent mass transfer near the solid surface at higher Schmidt numbers, while a wide range of frequencies play an important role near the free surface.

## 5. Visualization

Visualizations of instantaneous streamwise and surface-normal velocity components  $u^+$  and  $v^+$  at  $y^+ = 3.2$  and interfacial mass fluxes  $q^+$  for  $Sc = 1.0$  and 100 at a free surface are shown in Figs. 9 (a-d), respectively. In general, low mass-flux regions have streaky structures, which correspond to low-speed streaks in Fig. 9 (a). They become finer with the Schmidt number increased. On the other hand, high mass-flux regions are characterized by spotty structures. These structures are almost independent of the Schmidt number and even more highlighted at  $Sc = 100$ . It is also observed that the high mass-flux regions correspond to the regions where  $v$  is negative (see, the dotted regions in Figs. 9 (b-d)). This fact indicates that impingement of fresh liquid on the free surface is essential for the mass transfer. This is consistent with the high  $R_{cv}$  close to the free surface in Fig. 4 (b). The details of the transport mechanisms near the free surface are reported in Hasegawa and Kasagi (2007).

Visualizations of velocity and concentration fields near a solid surface are shown in Figs. 10 (a-d). At  $Sc = 1.0$ ,  $q^+$  is highly correlated with  $u^+$  in concurrence with high  $R_{cu}$  in Fig. 4 (a). At  $Sc = 100$ , distinct differences between the concentration fields close to the solid and free surfaces are found. The mass-flux fluctuations at the solid surface are quite calm compared with those near the free surface (compare Fig. 10 (d) with Fig. 9 (d)). Furthermore, both low and high mass-flux regions at the solid surface have streaky structures. By carefully comparing Fig. 10 (d) with Fig. 10 (c), it is also observed that the high mass-flux streaks at  $Sc = 100$  frequently lie about  $\Delta x^+ = 200$  downstream of the high mass-flux spots at  $Sc = 1.0$  (see, the dotted circles in Figs. 10 (c) and (d)). This is in a striking contrast with the distribution of the mass flux at the free surface shown in Fig. 9 (d), in which the concentration field quickly responds to the normal velocity fluctuation even at the high Schmidt number.

Totally, these visualizations support the results of the frequency analyses in Sec. 4. Namely, the velocity fluctuations at lower frequencies dominate the transport processes near the solid surface at higher Schmidt numbers.

## 6. Conclusions

Distinct differences are observed between the concentration fields near free and solid surfaces at high Schmidt numbers. Near the free surface, the concentration field quickly responds to the normal velocity fluctuation and the limiting behavior of the eddy diffusivity is almost independent of the Schmidt number. On the other hand, near the solid surface, the concentration field becomes insensitive to the normal velocity fluctuation and the limiting value of the eddy diffusivity is decreased by around 80 % with the Schmidt number increased from 1.0 to 100.

The present results show that the thickness of the region where  $E_d^+ \propto y^{+3}$  is decreased with increasing the Schmidt number and this region always lies in the diffusive sublayer where the turbulent transport is not significant. These results suggest that the analogy between momentum and mass transfer near the solid surface can not be used at high Schmidt numbers. These trends agree fairly well with the previous DNS results at moderate Schmidt numbers up to  $Sc = 10$  reported by Na and Hanratty (2000) and Seki et al. (2006).

The fundamental differences between the concentration fields near solid and free surfaces can be attributed to the difference of the spatial variation of the normal velocity fluctuation near the surfaces. According to the theoretical analysis of a one-dimensional advection-diffusion equation by McCready and Hanratty (1984), it is shown that near the free surface, where the normal velocity varies linearly with  $y$ , the frequency spectrum of the concentration fluctuation is independent of the Schmidt number. In contrast, near the solid surface, where the normal velocity varies quadratically with  $y$ , similar analysis (Shaw and Hanratty, 1977a) revealed that high-frequency concentration fluctuations are strongly damped with increasing the Schmidt number. The present results show quantitative agreement with the theoretical predictions at both free and solid surfaces.

Due to this damping effect, the contribution of high-frequency velocity fluctuations to turbulent mass transport are drastically decreased near a solid wall. This is the primary reason for the breakdown of the analogy between momentum and mass transfer. If we assume that the profile of the eddy diffusivity is unchanged from the present result even at higher Schmidt numbers, the prediction obtained by assuming

$E_d^+ = E_v^+$  overestimates the mass transfer rate about 5 %, 15% and 30% at  $Sc = 100$ , 1000 and 10000, respectively.

The damping effect also affects the instantaneous distribution of the mass flux at the solid surface. Visualization results show that high mass-flux regions at  $Sc = 100$  have highly elongated streaky structures and seem to happen a certain period of time after high mass-flux events occur at  $Sc = 1.0$ . More detailed investigation is required to clarify this issue. The present results underline the necessity of developing a mass transfer model which takes into account the damping effect near the solid surface.

### **Acknowledgement**

The present work was supported through the 21st Century COE Program, “Mechanical Systems Innovation,” by the Ministry of Education, Culture, Sports, Science and Technology, Japan.

## References

- [1] Batchelor, G. K., 1959. Small-scale variation of convected quantities like temperature in turbulent fluid – Part 1. General discussion and the case of small conductivity, *J. Fluid Mech.* 5, 113-133.
- [2] Calmet, I., Magnaudet, J., 1997. Large eddy simulation of high Schmidt number mass transfer in a turbulent channel flow, *Phys. Fluids* 9, 438-455.
- [3] Churchill, S. W., 1997. New simplified models and formulations for turbulent flow and convection, *A.I.Ch.E. Journal* 43, 1125-1140.
- [4] Germano, M., Piomelli, U., Moin, P. and Cabot, W., 1991. A dynamic mixed subgrid scale model and its application to turbulent recirculating flows, *Phys. Fluids A3*, 1760-1765.
- [5] Hanratty, T. J., 1991. Effect of gas flow on physical absorption. In: Wilhelms, Gulliver (Eds.), *Air-Water Gas Transfer*. ASCE (Civil Engineers), New York.
- [6] Hasegawa, Y. and Kasagi, N., 2005. Turbulent Mass Transfer Mechanism across a Contaminated Air-Water Interface. *Proceedings of Fourth International Symposium on Turbulent Shear Flow*, pp. 971-976.
- [7] Hasegawa, Y. and Kasagi, N., 2007. Hybrid DNS/LES of High Schmidt Number Mass Transfer Across Turbulent Air-Water Interface, *Int. J. Heat Mass Trans.*, submitted.
- [8] Kader, B. A., 1981. Temperature and Concentration Profiles in Fully Turbulent Boundary Layers, *Int. J. Heat Mass Trans.* 24 (9), 1541-1544.
- [9] Lombardi, P., De Angelis V. and Banerjee, S., 1996. Direct numerical simulation of near-interface turbulence in coupled gas-liquid flow, *Phys. Fluids* 8, 1643-1665.
- [10] McCready, M. J. and Hanratty, T. J., 1984. Concentration Fluctuations close to a Gas-Liquid Interface. *A.I.Ch.E. Journal* 30 (5), 816-817.
- [11] Moin A. S. and Yaglom, A. M., 1971. *Statistical Fluid Mechanics, Mechanics of Turbulence 1*, MIT Press, Cambridge, pp. 343.
- [12] Na, Y. and Hanratty, T. J., 2000. Limiting Behavior of Turbulent Scalar Transport Close to a Wall. *Int. J. Heat Mass Trans.* 43 (10), 1749-1758.
- [13] Papavassiliou, D. V. and Hanratty, T. J., 1997. Transport of a passive scalar in a turbulent channel flow. *Int. J. Heat Mass Trans.* 40 (6), 1303-1311.
- [14] Salvetti, M. V. and Banerjee, S., 1995. A priori tests of a new subgrid-scale model

for finite-difference large-eddy simulations, *Phys. Fluids* 7 (11), 2831-2847.

- [15] Seki, Y., Iwamoto, K., and Kawamura, H., 2006. Prandtl number effect on turbulence quantities through high spatial resolution DNS of turbulent heat transfer in a channel flow. *Proceedings of Turbulence, Heat and Mass Transfer*, CD-ROM.
- [16] Shaw, D. A. and Hanratty, T. J., 1977a. Influence of Schmidt Number on the Fluctuations of Turbulent Mass Transfer to a Wall. *A.I.Ch.E. Journal* 23 (2), 160-169.
- [17] Shaw, D. A. and Hanratty, T. J., 1977b. Turbulent Mass Transfer Rates to a Wall for Large Schmidt Number. *A.I.Ch.E. Journal* 23 (1), 28-37.
- [18] Tiselj, I., 2006. Role of the Sub-Kolmogorov Scales in the Near-Wall Turbulent Passive Scalar Transfer at High Prandtl Numbers. *Proceedings of Turbulence, Heat and Mass Transfer*, CD-ROM.
- [19] Zang, Y., Street, R. L. and Kosseff, J. R., 1993. A dynamic mixed subgrid scale model and its application to turbulent recirculating flows, *Phys. Fluids A* 5 (12), 3186-3196.

## Figure Captions

- Fig. 1 Computational domain and coordinate system (a) free surface, (b) solid surface.
- Fig. 2 Mean concentration profiles near free and solid surfaces.
- Fig. 3 Concentration fluctuations near (a) solid and (b) free surfaces.
- Fig. 4 Correlation coefficients (a)  $-R_{cu}$  and (b)  $R_{cv}$ .
- Fig. 5 Limiting behavior of eddy viscosity  $E_v$  and eddy diffusivity  $E_d$  near free and solid surfaces.
- Fig. 6 Limiting behavior of  $E_v^+ / y^{+3}$  and  $E_d^+ / y^{+3}$  near solid surfaces.
- Fig. 7 Frequency spectra of interfacial mass flux  $q$  and coefficients  $\gamma$  and  $\beta$  of Taylor expansion of normal velocity fluctuation near (a) solid and (b) free surfaces.
- Fig. 8 Frequency co-spectra of turbulent mass flux  $\overline{c'v'}$  at  $y^+ = 3.2$  from (a) solid and (b) free surfaces.
- Fig. 9 Visualization of velocity and concentration fields near a free surface.  
(a): streamwise velocity  $u^+$ , (b): surface-normal velocity  $v^+$  at  $y^+ = 3.2$  and interfacial mass flux  $q^+$  at (c):  $Sc = 1.0$  and (d):  $Sc = 100$ .
- Fig. 10 Visualization of velocity and concentration fields near a solid surface.  
(a): streamwise velocity  $u^+$ , (b): surface-normal velocity  $v^+$  at  $y^+ = 3.2$  and interfacial mass flux  $q^+$  at (c):  $Sc = 1.0$  and (d):  $Sc = 100$ .

Table 1 Number of modes, number of grid points and grid spacings

		Region	$k_x, k_y$ or $N_y, k_z$	$\Delta x^+$	$\Delta y^+$	$\Delta z^+$
Velocity	DNS	$0 < y^+ < 150$	64, 129, 64	18.4	0.01 ~ 1.23	7.2
Case 1	DNS	$0 < y^+ < 11.3$	192, 34, 192	6.1	0.01 ~ 0.62	2.4
	Buffer	$11.3 < y^+ < 21.6$	192, 15, 192	6.1	0.66 ~ 0.85	2.4
	LES	$21.6 < y^+ < 150$	64, 144, 64	18.4	0.86 ~ 1.23	7.2
Case 2	DNS	$0 < y^+ < 22.8$	192, 50, 192	6.1	0.01 ~ 0.79	2.4
	Buffer	$22.8 < y^+ < 35.4$	192, 15, 192	6.1	0.81 ~ 0.85	2.4
	LES	$35.4 < y^+ < 150$	64, 122, 64	18.4	0.86 ~ 1.23	7.2
Velocity	DNS	$0 < y^+ < 150$	64, 289, 64	18.4	0.002 ~ 0.38	7.2
Case 3	DNS	$0 < y^+ < 16.5$	512, 94, 512	2.3	0.002 ~ 0.34	0.9
	Buffer	$16.5 < y^+ < 21.6$	512, 15, 512	2.3	0.35 ~ 0.38	0.9
	LES	$21.6 < y^+ < 150$	64, 324, 64	18.4	0.002 ~ 0.38	7.2

Table 2 Limiting values at free and solid surfaces

		<b>Sc = 1.0</b>	<b>Sc = 10</b>	<b>Sc = 100</b>
<b>Solid surface</b>	$\sqrt{s_1^2} / Sc$	0.402 (present) 0.403 (Na & Hanratty)	0.393 (Na & Hanratty)	0.325 (present)
	$A_3 \times 10^{-3}$	0.722 (present) 0.730 (Na & Haratty)	0.503 (Na & Hanratty)	0.118 (present)
	$B_3 \times 10^{-3}$	0.728x10 <sup>-3</sup> (present), 0.790x10 <sup>-3</sup> (Na & Hanratty)		
	${}^tSc = B_3 / A_3$	0.992 (present) 1.08 (Na & Haratty)	1.57 (Na & Hanratty) 1.47 (Seki et al.)	6.19 (present)
<b>Free surface</b>	$\sqrt{s_1^2} / Sc$	0.590 (present)	-	0.654 (present)
	$A_2$	0.0197 (present)	-	0.0247 (present)
	$B_1$	0.0335 (present)		

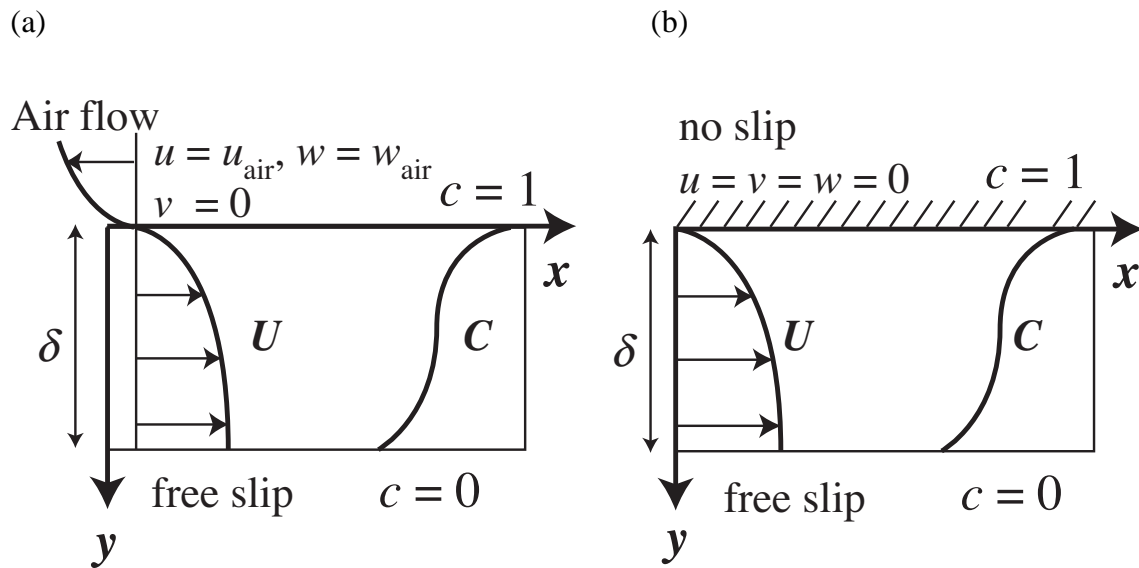


Fig. 1 Computational domain and coordinate system  
 (a) free surface, (b) solid surface.

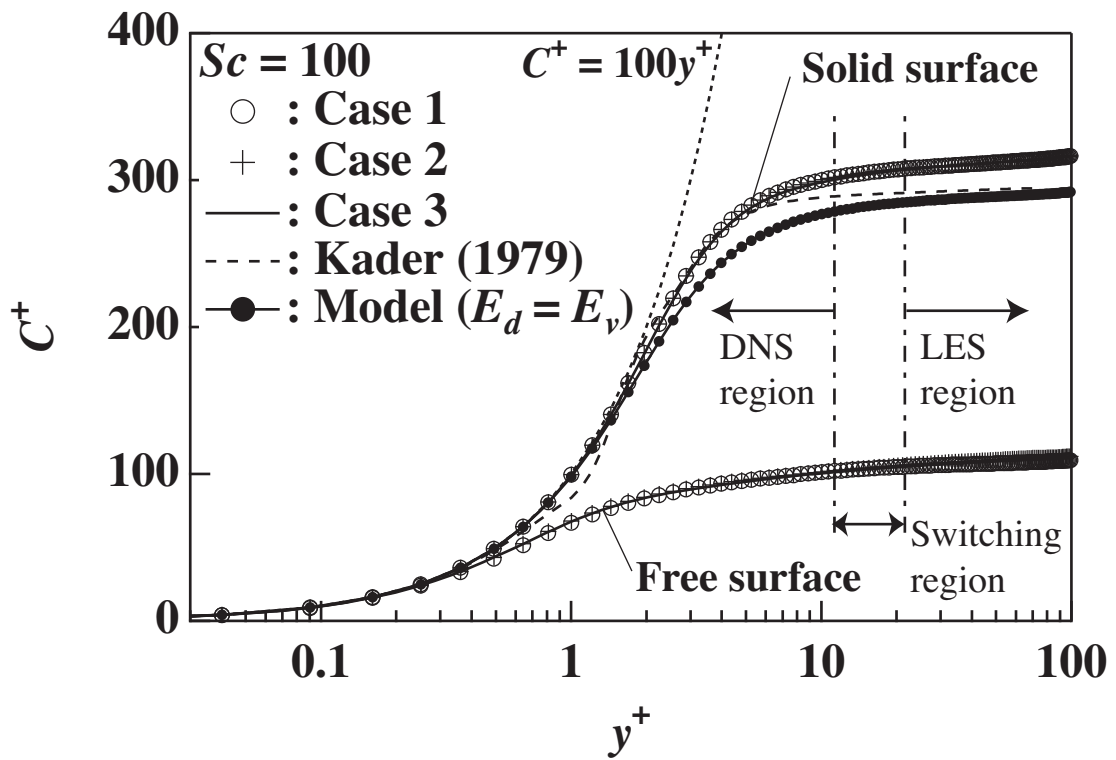
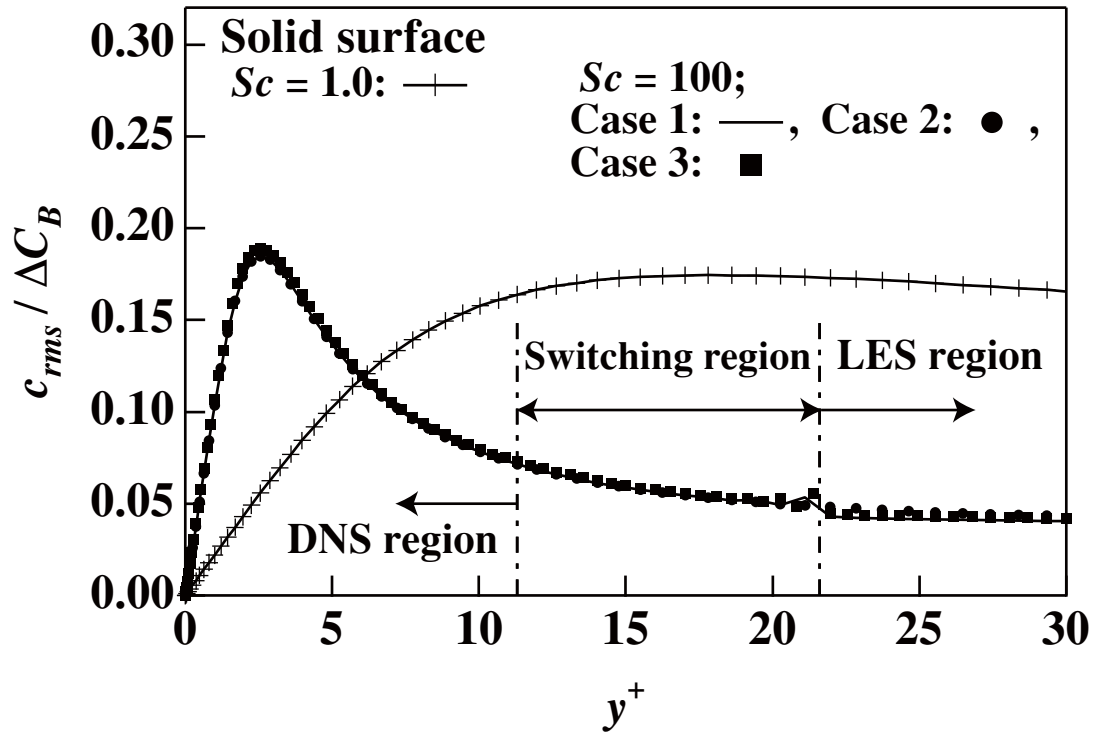


Fig. 2 Mean concentration profiles near free and solid surfaces.

(a)



(b)

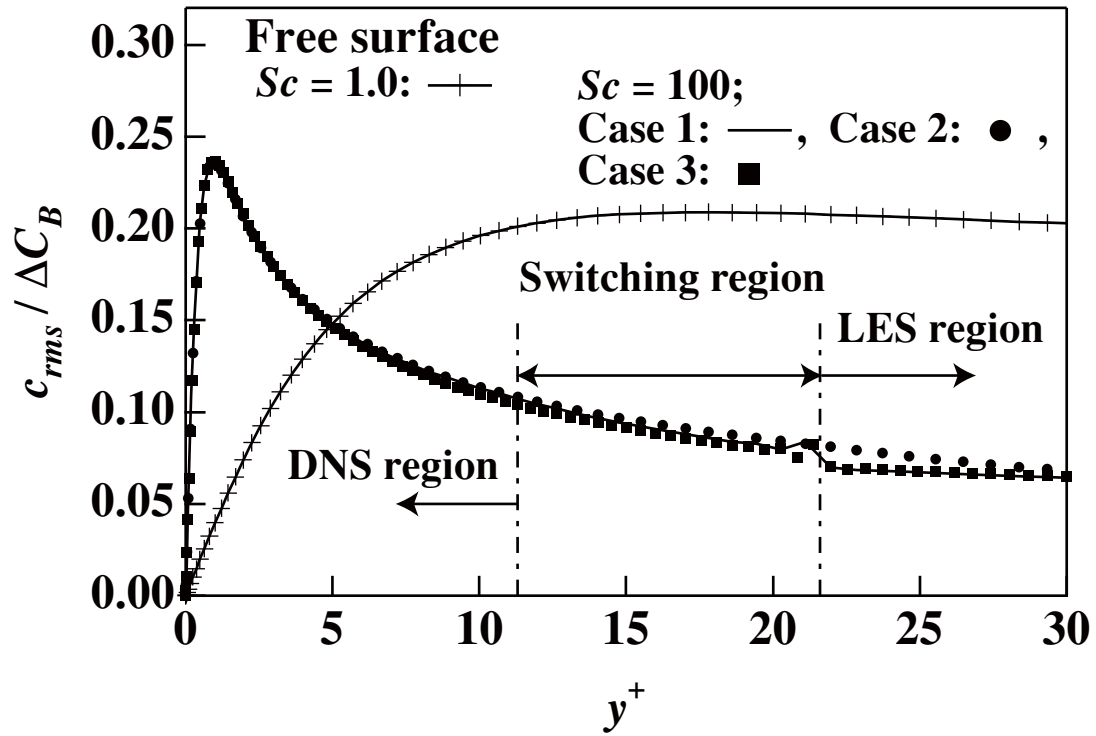
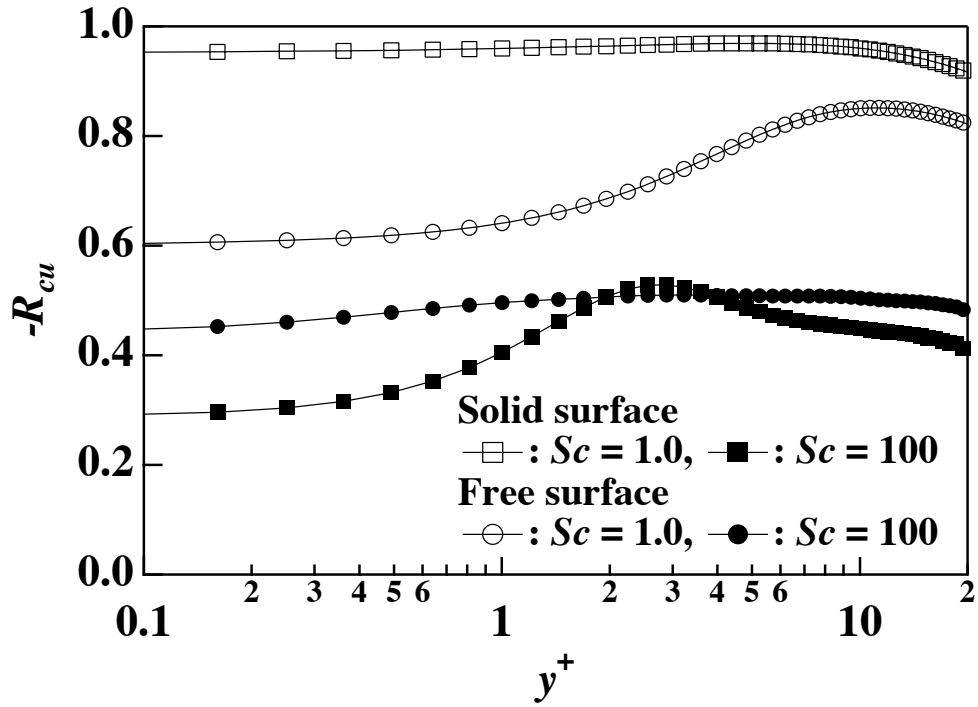


Fig. 3 Concentration fluctuations near (a) solid and (b) free surfaces.

(a)



(b)

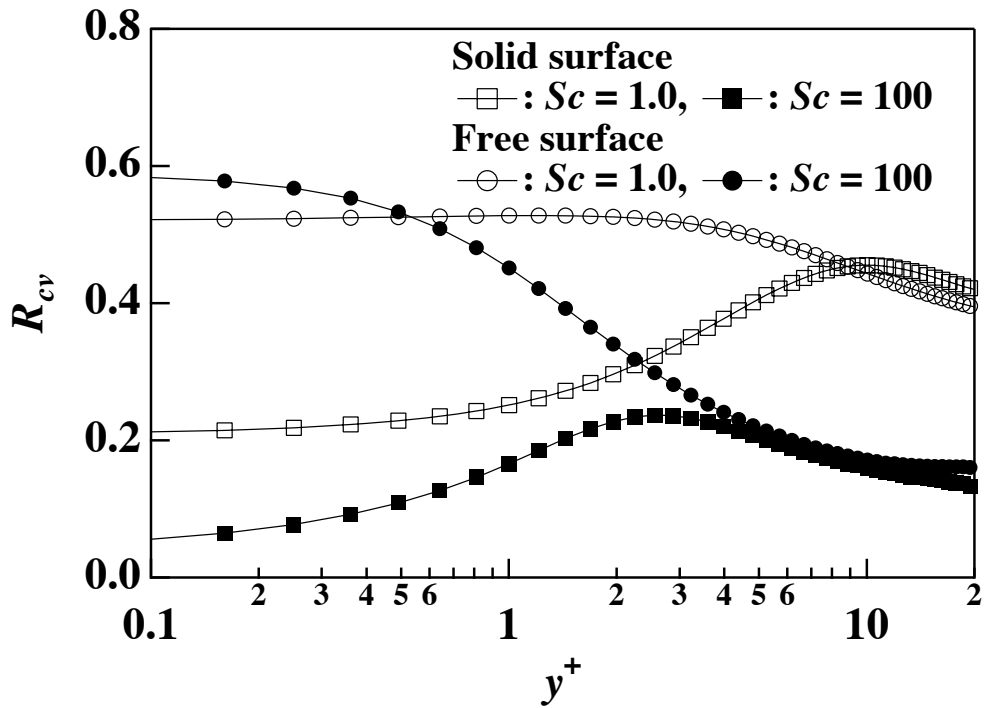


Fig. 4 Correlation coefficients (a)  $-R_{cu}$  and (b)  $R_{cv}$ .

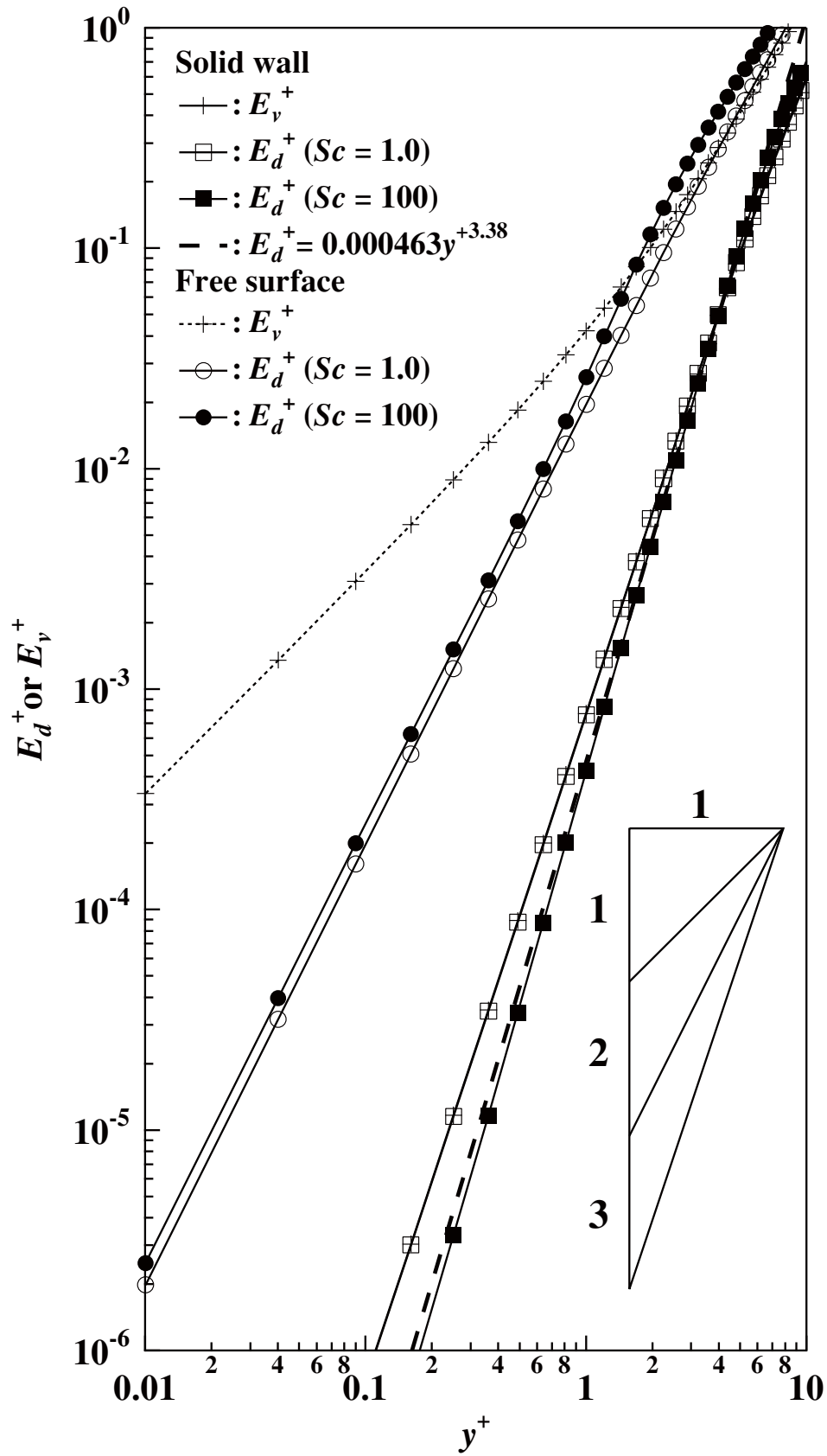


Fig. 5 Limiting behavior of eddy viscosity  $E_v^+$  and eddy diffusivity  $E_d^+$  near free and solid surfaces.

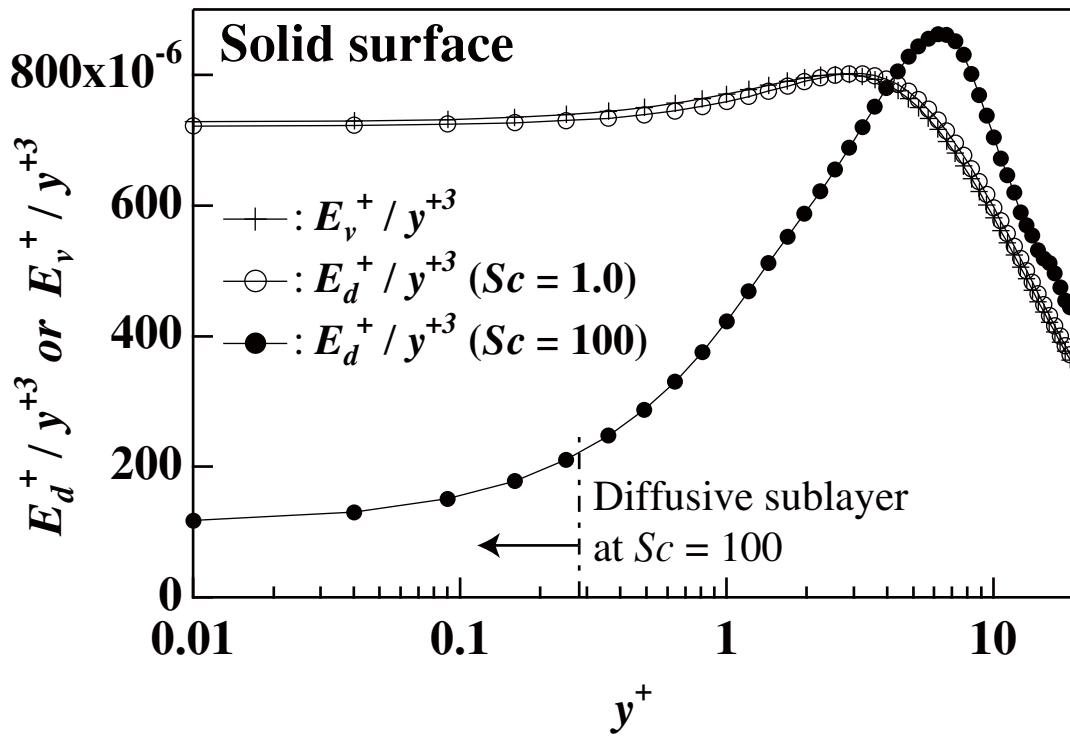


Fig. 6 Limiting behavior of  $E_v^+ / y^{+3}$  and  $E_d^+ / y^{+3}$  near solid surfaces.

(a)

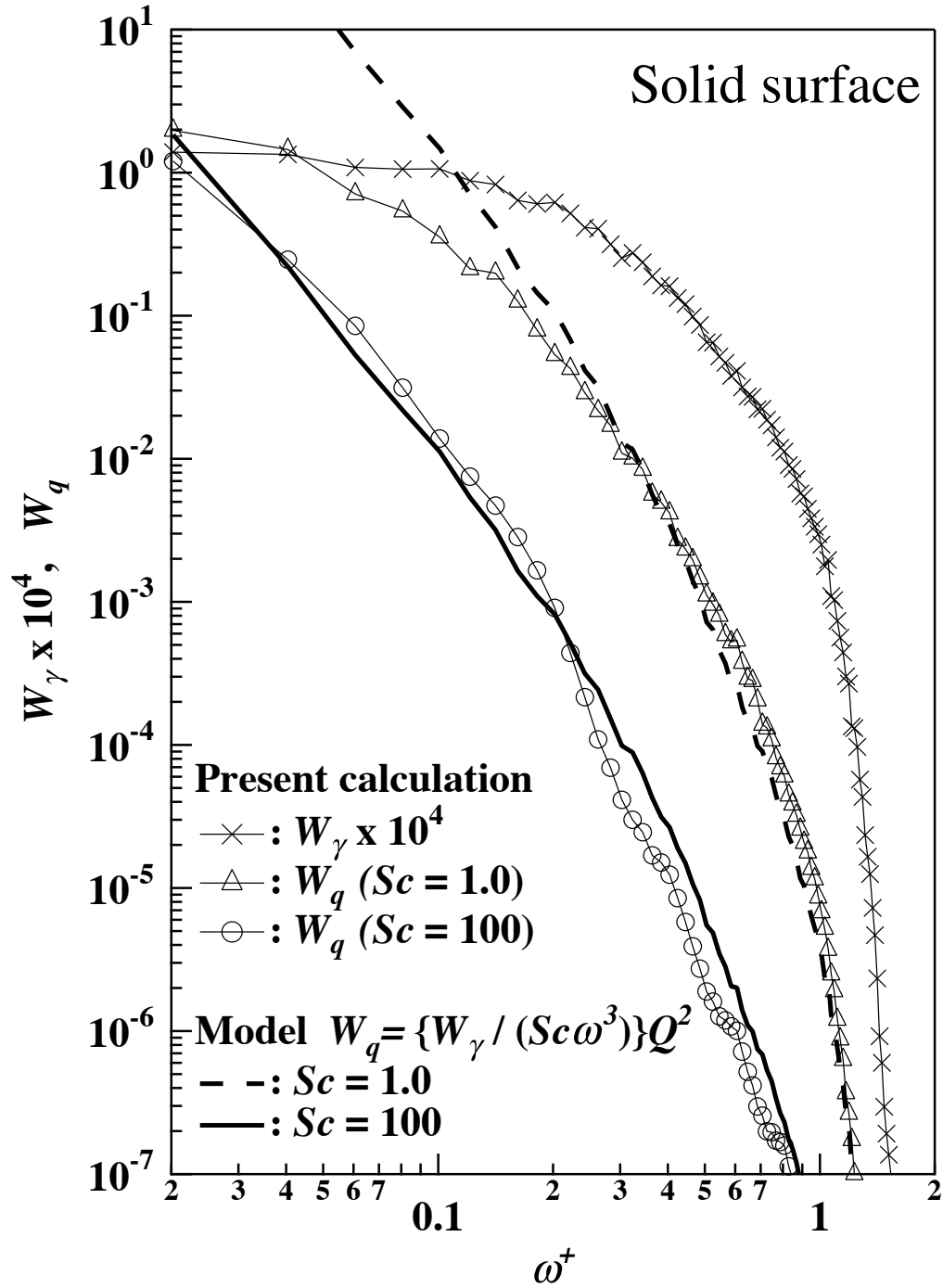


Fig. 7 Frequency spectra of interfacial mass flux  $q$  and coefficients  $\gamma$  and  $\beta$  of Taylor expansion of normal velocity fluctuation near  
(a) solid and (b) free surfaces.

(b)

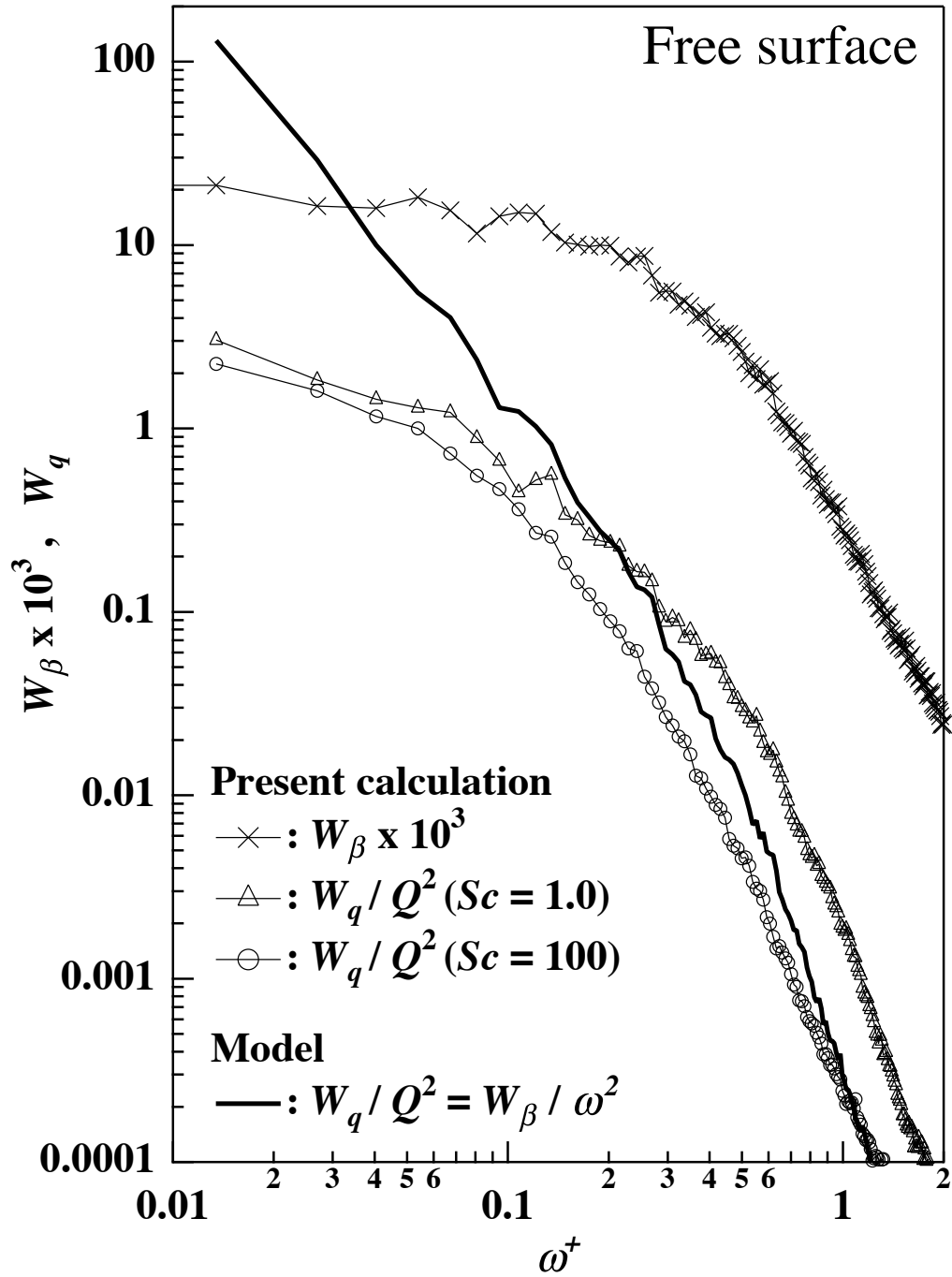
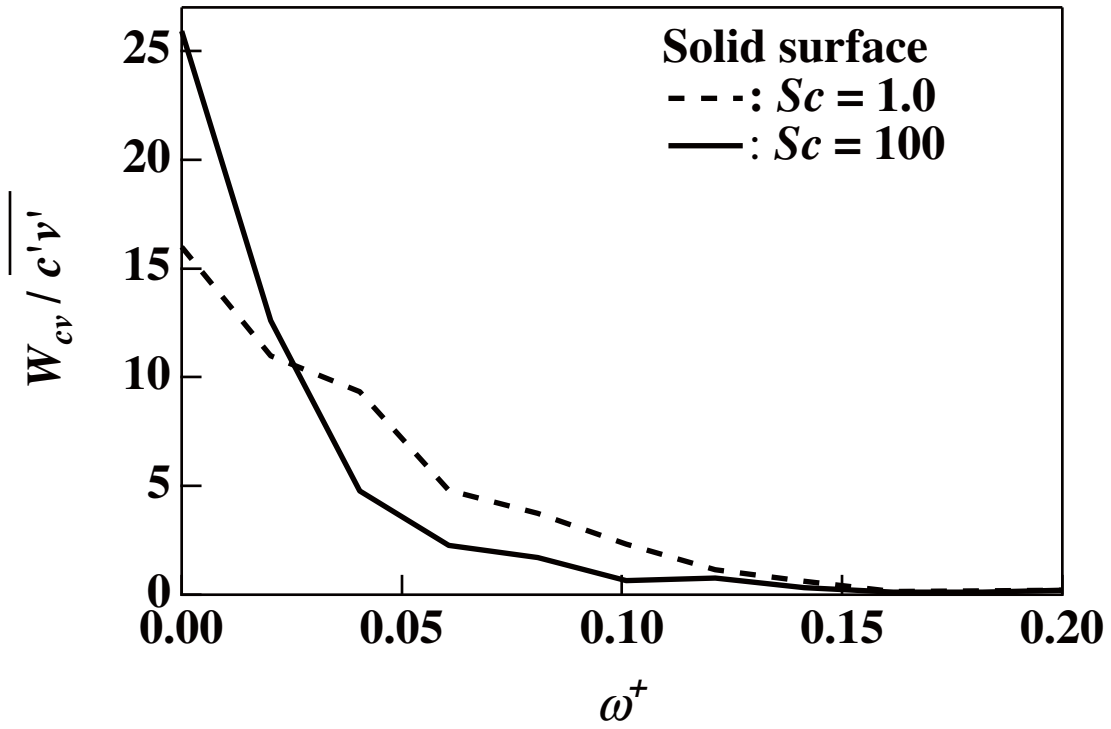


Fig. 7 continued.

(a)



(b)

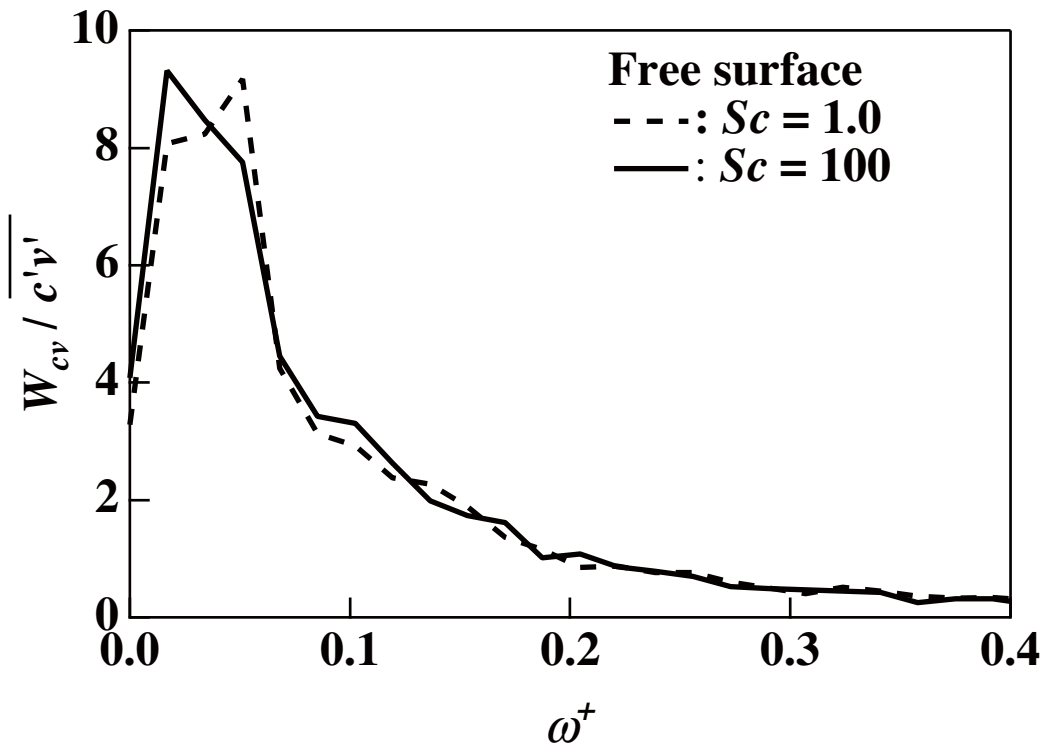


Fig. 8 Frequency cospectra of turbulent mass flux  $\overline{c'v'}$  at  $y^+ = 3.2$  from (a) solid and (b) free surfaces.

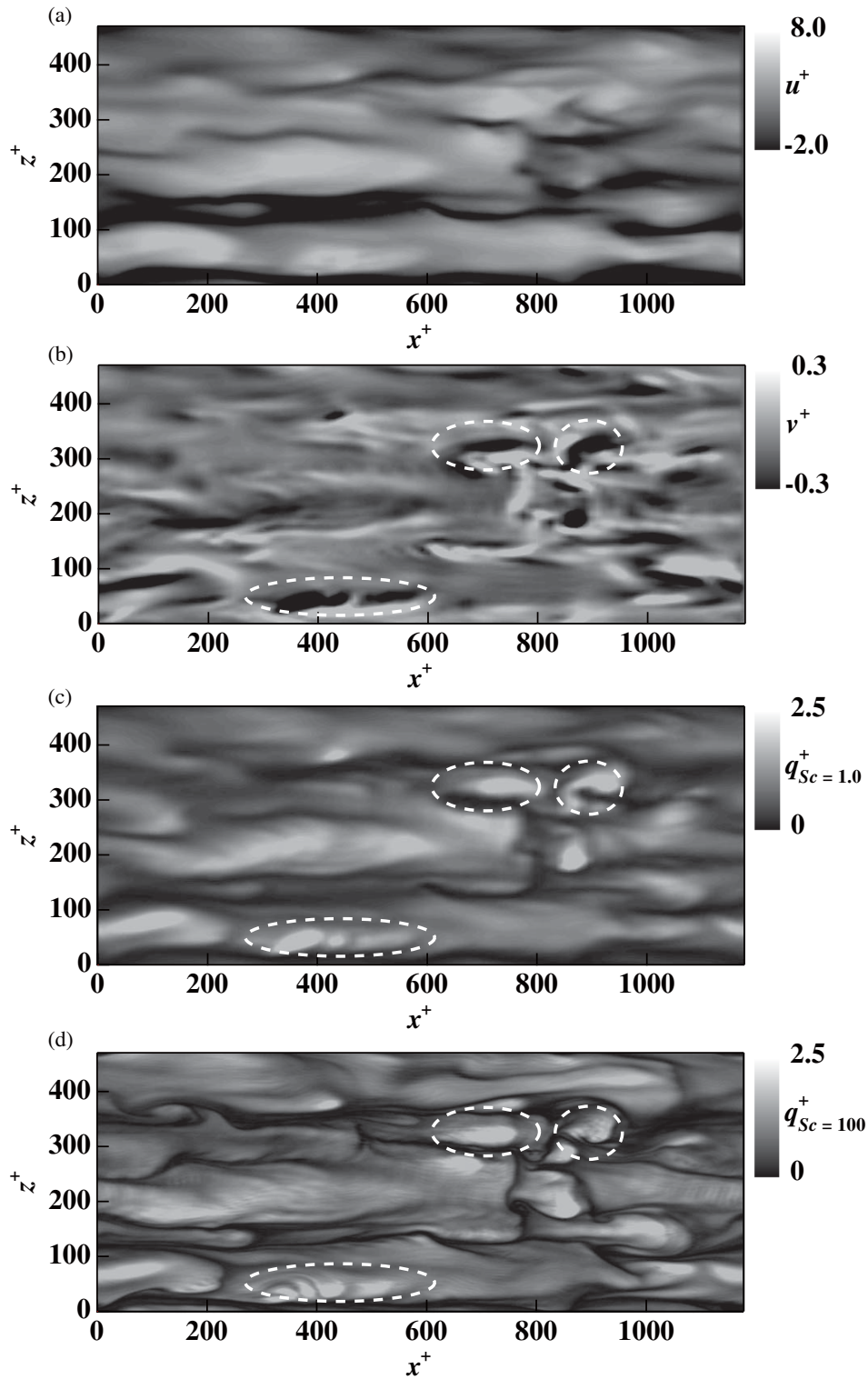


Fig. 9 Visualization of velocity and concentration fields near a free surface.  
 (a): streamwise velocity  $u^+$ , (b): surface-normal velocity  $v^+$  at  $y^+ = 3.2$  and  
 interfacial mass flux  $q^+$  at (c):  $Sc = 1.0$  and (d):  $Sc = 100$ .

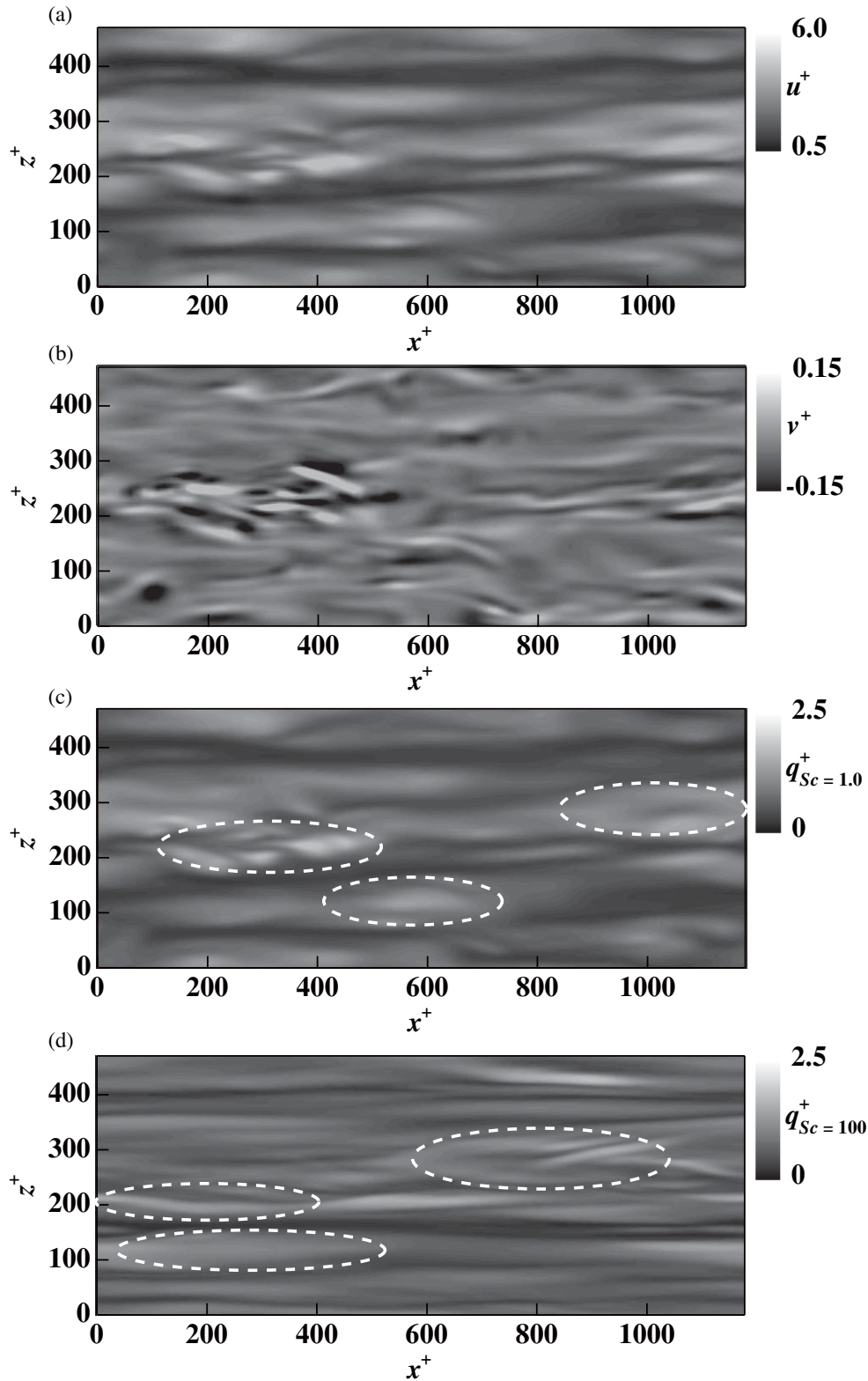


Fig. 10 Visualization of velocity and concentration fields near a solid surface. (a): streamwise velocity  $u^+$ , (b): surface-normal velocity  $v^+$  at  $y^+ = 3.2$  and interfacial mass flux  $q^+$  at (c):  $Sc = 1.0$  and (d):  $Sc = 100$ .